

Finite, Intense Accretion Bursts from Tidal Disruption of Stars on Bound Orbits

Kimitake Hayasaki^{1,2,3*}, Nicholas Stone² and Abraham Loeb²

¹*Department of Astronomy, Kyoto University, Kitashirakawa-Oiwake-cho, Sakyo-ku, Kyoto 606-8502, Japan*

²*Harvard-Smithsonian Center for Astrophysics, 60 Garden Street, Cambridge, MA 02138, USA*

³*Korea Astronomy and Space Science Institute, Daedeokdaero 776, Yuseong, Daejeon 305-348, Korea*

ABSTRACT

We study accretion processes for tidally disrupted stars approaching supermassive black holes on bound orbits, by performing three dimensional Smoothed Particle Hydrodynamics simulations with a pseudo-Newtonian potential. We find that there is a critical value of the orbital eccentricity below which all the stellar debris remains bound to the black hole. For high but sub-critical eccentricities, all the stellar mass is accreted onto the black hole in a finite time, causing a significant deviation from the canonical $t^{-5/3}$ mass fallback rate. When a star is on a moderately eccentric orbit and its pericenter distance is deeply inside the tidal disruption radius, there can be several orbit crossings of the debris streams due to relativistic precession. This dissipates orbital energy in shocks, allowing for rapid circularization of the debris streams and formation of an accretion disk. The resultant accretion rate greatly exceeds the Eddington rate and differs strongly from the canonical rate of $t^{-5/3}$. By contrast, there is little dissipation due to orbital crossings for the equivalent simulation with a purely Newtonian potential. This shows that general relativistic precession is crucial for accretion disk formation via circularization of stellar debris from stars on moderately eccentric orbits.

Key words: accretion, accretion discs – black hole physics – gravitational waves – galactic: nuclei – hydrodynamics

1 INTRODUCTION

Supermassive black holes (SMBHs) larger than $10^5 M_\odot$ are now known to exist ubiquitously in galactic nuclei. SMBHs in nearby galaxies can be studied dynamically, whereas in more distant galaxies only the $\sim 1\%$ of SMBHs undergoing major accretion episodes can be easily observed. The tidal disruption and subsequent accretion of a star by a SMBH, although intrinsically a rare event, is of observational interest as a way to probe dormant SMBHs in the local universe, because it can produce a powerful flare in excess of the Eddington luminosity (Carter & Luminet 1983; Rees 1988; Evans & Kochanek 1989; Strubbe & Quataert 2009). These events are also of interest to low-frequency gravitational wave astronomy, as the stellar dynamical processes which funnel stars into the low angular momentum orbits necessary for tidal disruption events (TDEs) are similar to those which produce the extreme-mass ratio inspiral of a stellar-mass compact object onto a SMBH (Frank & Rees 1976; Wang & Merritt 2004; Madigan et al. 2011). TDEs have also been considered as part of the means by which

a seed black hole grows into a SMBH (Zhao et al. 2002; Miralda-Escudé & Kollmeier 2005; Bromley et al. 2012). All of these aspects of stellar tidal disruption have motivated past studies of TDEs.

The traditional picture of a TDE proceeds as follows: a star at large separation (~ 1 pc) approaches a SMBH on a nearly parabolic orbit. After the star is tidally disrupted by the black hole, half the stellar debris becomes gravitationally bound to the SMBH, because it loses orbital energy inside the tidal radius. The bound debris falls back, and, after circularizing due to collisional shocks with other gas streams, accretes onto the black hole. Kepler’s third law implies that the mass return rate decays with a $-5/3$ power of time (Rees 1988; Phinney 1989), asymptotically approaching zero. This simple analytic picture has been validated to the first order of approximation by hydrodynamical simulations (Evans & Kochanek 1989), albeit with deviations from this law at early times (Lodato et al. 2009). Similar power-law behavior for the flare lightcurve is often assumed (i.e. $L \propto \dot{M}$), although here the theoretical evidence is less clear (Lodato & Rossi 2011).

All-sky surveys in the X-ray and UV have so far observed 13 candidate tidal disruption flares

* E-mail: kimi@kusastro.kyoto-u.ac.jp; kimi@kasi.re.kr

(Komossa & Bade 1999; Grupe et al. 1999; Greiner et al. 2000; Komossa et al. 2004; Halpern et al. 2004; Dogiel et al. 2009; Maksym et al. 2010; Bloom et al. 2011; Burrows et al. 2011). The observed light curves are in reasonable agreement with the theoretically predicted mass fallback rate of $t^{-5/3}$, although some show deviations (Burrows et al. 2011) and the number of samples is sufficiently small to make detailed testing of theoretical models difficult. A smaller number of strong TDE candidates have been found at optical wavelengths (van Velzen et al. 2011; Gezari et al. 2012). Notably, two of the best-sampled TDEs differ strongly from the canonical theoretical picture: one possesses relativistic jets (Bloom et al. 2011; Zauderer et al. 2011), and the other lacks hydrogen lines in its spectra (Gezari et al. 2012).

It has been inferred from observations that the event rate of tidal disruption is $\sim 10^{-5}\text{yr}^{-1}$ per galaxy (Donley et al. 2002). This observed rate is in rough agreement with uncertain theoretical rate estimates. In the standard scenario, stars are supplied to the SMBH by two body scattering, on a stellar relaxational timescale. Stars with angular momentum less than a critical value are in the phase space “loss cone” and are tidally destroyed on a dynamical time. Theoretical calculations indicate this rate to be $\sim 10^{-4} - 10^{-6} \text{ yr}^{-1}$ for Milky Way-like galaxies, and that the peak flux into the loss cone comes from parsec scales. This motivates the assumption of nearly parabolic orbits (Magorrian & Tremaine 1999; Wang & Merritt 2004).

However, there are alternate sources of TDEs distinct from the standard two-body scattering model. Many of these feed stars to the SMBH at lower eccentricity. Our aim here is to quantify through hydrodynamical numerical simulations how the observable properties of tidal disruptions of stars on eccentric orbits deviate from the standard ones. In § 2, we describe numerical procedures for simulating TDEs. We then analyze results of our simulations in § 3. In § 4 we consider nonstandard sources of TDEs and whether they can supply stars on low eccentricity orbits to a SMBH. Finally, § 5 is devoted to summary and discussion of our scenario.

2 NUMERICAL METHOD

In this section, we describe our procedures for numerically modeling the tidal disruption of stars on bound orbits. The simulations presented below were performed with a three-dimensional (3D) SPH code, which is a particle method that divides the fluid into a set of discrete “fluid elements” (i.e. particles), and is flexible in setting various initial configurations. The code is based on a version originally developed by Benz (1990); Benz et al. (1990); Bate et al. (1995) and has been extensively used by many papers (e.g., Okazaki et al. (2002); Hayasaki et al. (2007)). The SPH equations with the standard cubic-spline kernel are integrated using a second-order Runge-Kutta-Fehlberg integrator with individual time steps for each particle (Bate et al. 1995), which results in enormous computational time savings when a large range of dynamical timescales are involved. In simulations shown in this paper, we adopt standard SPH artificial viscosity parameters $\alpha_{\text{SPH}} = 1$ or $\beta_{\text{SPH}} = 2$, unless otherwise noted. We have performed two-stage simulations. We model a star as a polytropic gas sphere in hydrostatic equilibrium. The tidal

disruption process is modeled by setting the star in motion through the gravitational field of an SMBH.

2.1 Formation of polytropes

In our code, the polytrope is composed of an ensemble of gas particles, each of which has a mass chosen to be $10^{-5}M_{\odot}$ with a variable smoothing length. The particles are initially uniformly distributed in a spherical fashion, with an initial temperature $T_{\text{ini}} = 1.2 \times 10^6 K$. The initial spherical gas cloud is allowed to collapse under self-gravity using the polytropic equation of state:

$$P = K\rho^{1+1/n}, \quad (1)$$

where n is the polytropic index and K is assumed to be kept constant throughout the collapse. Note that $n = 1.5$ corresponds to $\gamma = 5/3$. The simulations continue over five dynamical times, where the dynamical time is defined by

$$\Omega_*^{-1} \equiv \sqrt{\frac{r_*^3}{Gm_*}} \simeq 5.1 \times 10^{-5} \left(\frac{r_*}{R_{\odot}}\right)^{3/2} \left(\frac{M_{\odot}}{m_*}\right)^{1/2} \text{ yr}, \quad (2)$$

where G is Newton’s constant and r_* and m_* are the stellar radius and mass, respectively.

Fig. 1 shows the radial density profile of the polytropic gas sphere at $4.4\Omega_*^{-1}$, where the magnitude of ratio of thermal and gravitational energy becomes ~ 0.5 . While circle marks show the radial density profile obtained from the SPH simulations, the solid line shows the profile obtained by numerically solving the Lane-Emden equation:

$$\frac{1}{\xi^2} \frac{d}{d\xi} \left(\xi^2 \frac{d\theta}{d\xi} \right) = -\theta^n, \quad (3)$$

where we define as dimensionless quantities, $\xi = r/r_c$ with

$$r_c = \left(\frac{K(n+1)}{4\pi G} \rho_c^{1/n-1} \right)^{1/2}, \quad (4)$$

and $\theta^n = \rho/\rho_c$ with the central density ρ_c . With boundary conditions that $\theta = 1$ and $d\theta/d\xi = 0$ at $\xi = 0$ and $\theta = 0$ and $\xi = R_{\odot}/r_c$ at the surface of the star for 1 solar mass sun-type star, we obtained that $\rho_c \simeq 8.4 \text{ g cm}^{-3}$, $r_c \simeq 0.27R_{\odot}$ and $K \simeq 2.5 \times 10^{15}$.

2.2 Initial configuration

A star is tidally disrupted when the tidal force of the black hole acting on the star is stronger than the self-gravitational force of the star. The radius where these two forces balance is defined as the tidal disruption radius by

$$r_t = \left(\frac{M_{\text{BH}}}{m_*} \right)^{1/3} r_*, \quad (5)$$

where M_{BH} is the black hole mass.

Fig. 2 shows a density map of the polytropic gas sphere at $4.4\Omega_*^{-1}$. The left panel shows the column density of polytropic sphere with $n = 1.5$ over a range of five orders of magnitude. The right panel shows the star-black hole system on the x - y plane, where both axes are normalized by r_t and the black hole is put on the origin of the system. The initial position of the star is given by $\mathbf{r}_0 = (r_0 \cos \phi_0, r_0 \sin \phi_0, 0)$, where $|r_0| = r_0$ is the radial distance from the black hole and ϕ_0 shows the angle between x -axis and \mathbf{r}_0 . The star

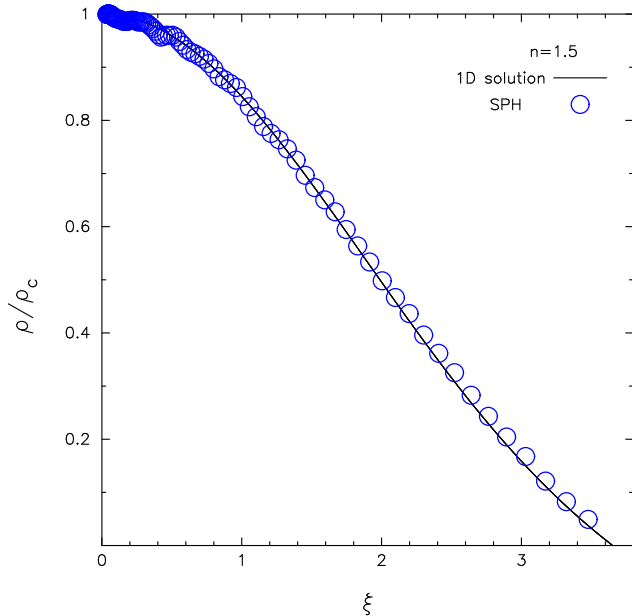


Figure 1. The radial density distribution of the polytropic gas sphere with $n = 1.5$. The solid line and circle marks show the solution for the Lane-Emden equation with $n = 1.5$ and the solution derived from the SPH simulation, respectively. The density is normalized by the central density $\rho_c = 8.4 \text{ g cm}^{-3}$ and $\xi = r/r_c$, where $r_c \simeq 0.27R_\odot$.

within a small square is zoomed out to the whole left panel. Note that the stellar size on the plot has been scaled up by a factor of a few for visual clarity.

The motion of a test particle in the central SMBH potential $U(r)$ admits two conserved quantities. The radial velocity and angular velocity are given by energy conservation and angular momentum conservation as (Landau & Lifshitz 1969)

$$\dot{r} = \sqrt{2(\epsilon - U(r)) - \frac{l^2}{r^2}}, \quad (6)$$

$$\dot{\phi} = \frac{l}{r^2}, \quad (7)$$

where ϵ and l are the specific energy and the specific angular momentum, respectively. For bound orbits,

$$\epsilon = \frac{(r_p/r_a)^2 U(r_p) - U(r_a)}{(r_p/r_a)^2 - 1}, \quad (8)$$

$$l = \sqrt{2r_p^2(\epsilon - U(r_p))} = \sqrt{2r_a^2(\epsilon - U(r_a))}, \quad (9)$$

where r_p and r_a are the pericenter distance and the apocenter distance, respectively. Therefore, the initial velocity vector is given by $\mathbf{v}_0 = (\dot{r}(r_0) \cos \phi_0 - r_0 \dot{\phi}(\phi_0) \sin \phi_0, \dot{r}(r_0) \sin \phi_0 + r_0 \dot{\phi}(\phi_0) \cos \phi_0, 0)$.

In our simulations, the black hole is represented by a sink particle with the appropriate gravitational mass M_{BH} . All gas particles that fall within a specified accretion radius are accreted by the sink particle. We set the accretion radius of the black hole as equal to the Schwarzschild radius $r_s = 2GM_{\text{BH}}/c^2$, with c being the speed of light.

2.3 Treatment of relativistic precession

In order to treat approximately the relativistic precession of a test particle in the Schwarzschild metric, we incorporate into our SPH code the following pseudo-Newtonian potential (Wegg 2012):

$$U(r) = -\frac{GM_{\text{BH}}}{r} \left[c_1 + \frac{1 - c_1}{1 - c_2(r_s/2r)} + c_3 \frac{r_s}{2r} \right], \quad (10)$$

where we adopt that $c_1 = (-4/3)(2 + \sqrt{6})$, $c_2 = (4\sqrt{6} - 9)$, and $c_3 = (-4/3)(2\sqrt{6} - 3)$. Equation (10) reduces to the Newtonian potential when $c_1 = 1$ and $c_2 = c_3 = 0$, while it reduces to the well-known Paczyński & Wiita pseudo-Newtonian potential (Paczyński & Wiita 1980) when $c_1 = c_3 = 0$. Note that equation (10) includes no higher-order relativistic effects such as the black hole spin or gravitational wave emission.

Fig. 3 tests how accurately the SPH particles composing the star follow test particle motion in the Schwarzschild metric. Specifically, the figure shows the motion of three particles orbiting the black hole with $(e, \beta) = (0.8, 5)$, where $\beta = r_t/r_p$ is the penetration factor which determines how deeply the star plunges into the black hole potential inside the tidal disruption radius. The central point and dashed circle show the black hole and the tidal disruption radius, respectively. The small crosses, dotted line, and solid line represent the geodesics of the Schwarzschild metric, orbits of the test particle under the pseudo-Newtonian potential, and those of a SPH particle in the simulation of Model 2a, respectively.

During the first one and a half orbits, the test particle is in good agreement with the corresponding geodesic. The subsequent deviation from the geodesic is due to the relatively low eccentricity and high β , since equation (10) is tailored to parabolic orbits with lower β (Wegg 2012) (see also Fig. 4). The first three and half orbits of the test particle are in rough agreement with corresponding orbits of the SPH particle. Subsequent large deviations originate from orbital circularization via shock-induced energy dissipation (see Section 3.2 in detail), and although our model becomes unreliable at this point, it is clear that stream crossing is leading to rapid energy dissipation.

Fig. 4 shows the dependence of the error rate on the eccentricity of a test particle moving under the pseudo-Newtonian potential given by equation (10). The error rate is defined by $(\Delta\phi_{\text{GR}} - \Delta\phi_{\text{PN}})/\Delta\phi_{\text{GR}} \times 100$, where $\Delta\phi_{\text{GR}}$ and $\Delta\phi_{\text{PN}}$ are the precession angles corresponding to equation (2) and (4) of Wegg (2012), respectively, with a given specific angular momentum, specific orbital energy, and equation (10). The solid line, dashed line, and dotted line show error rates of an orbit with $r_p = 3r_s$ ($\beta \approx 7.9$), $r_p = 5r_s$ ($\beta \approx 4.7$), and $r_p = 10r_s$ ($\beta \approx 2.4$), respectively, where $r_t \approx 23.6r_s$ is adopted. The error rate increases as the eccentricity is lower and the penetration factor is higher. From the figure, the error rate is estimated to be roughly 15% for $e = 0.8$ with $\beta = 5$, while it is less than 1% for $e \gtrsim 0.95$ with arbitrary β .

2.4 Numerical models

We have performed eight simulations of tidal disruption events with different parameters. The common param-

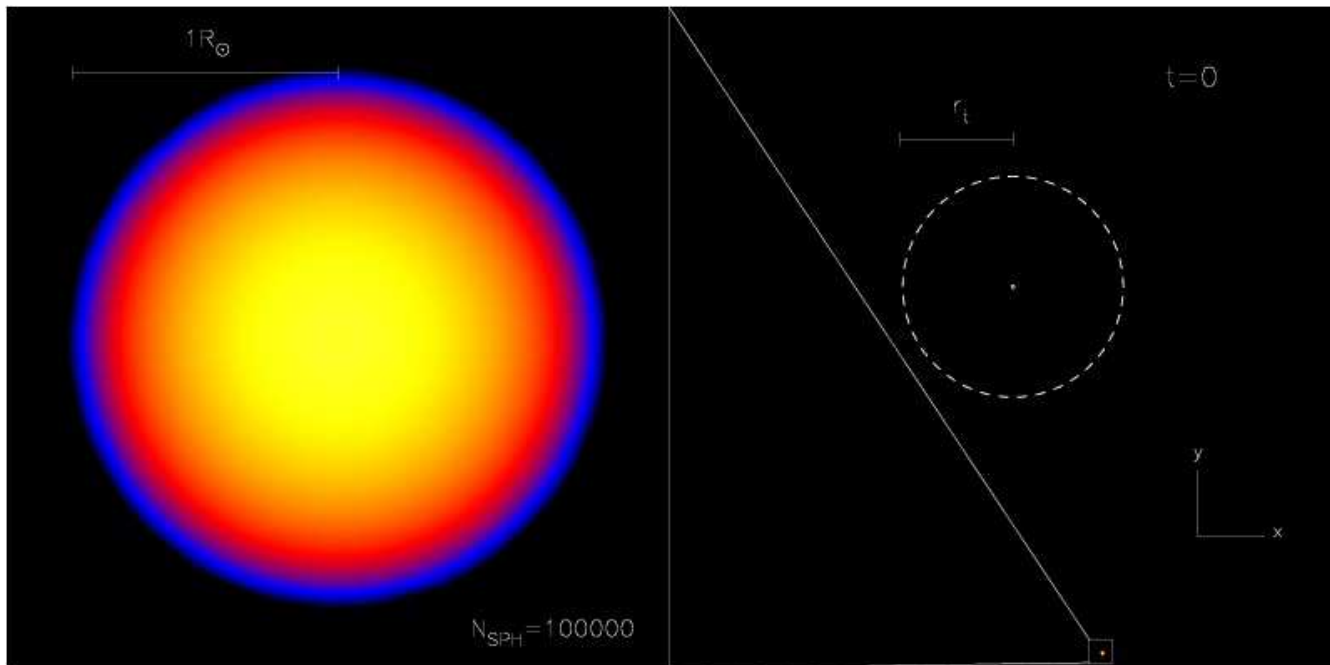


Figure 2. Initial configuration of our simulations. The left panel shows a density map of the polytropic gas sphere with $n = 1.5$. Its radius is $1R_{\odot}$ and the number of SPH particles N_{SPH} are annotated in the right-bottom corner of the panel. The panel on the right-hand-side shows the initial position of the star on the x - y plane. The small square corresponds to the entire left panel, the dashed circle shows the tidal disruption radius r_t and the black hole is positioned at the center. The simulation run time t in the right-top corner is normalized by Ω_*^{-1} . In the right panel, the star is initially located at $(r_0 \cos \phi_0, r_0 \sin \phi_0)$, where $r_0 = 3r_t$ and $\phi_0 = -0.4\pi$.

Table 1. The first column shows each simulated scenario. The second, third, fourth, and fifth columns are the penetration factor $\beta = r_p/r_T$, the initial orbital eccentricity e_* , the initial semi-major axis a_* , and the radial distance between the black hole and the initial position of the star, respectively. The last column describes the remark for each model.

Model	$\beta = r_t/r_p$	e_*	$a_* [r_t]$	$r_0 [r_t]$	Remarks
1a	1	1.0	—	3	Newtonian
1b	1	1.0	—	3	Pseudo-Newtonian
1c	5	1.0	—	3	Newtonian
1d	5	1.0	—	3	Pseudo-Newtonian
2a	5	0.8	1.0	1.8	Pseudo-Newtonian
2b	5	0.8	1.0	1.8	Newtonian
3a	1	0.98	50.0	3	Pseudo-Newtonian
3b	5	0.98	10.0	3	Pseudo-Newtonian

ters through all of simulations are following: $m_* = 1M_{\odot}$, $r_* = 1R_{\odot}$, $M_{\text{BH}} = 10^6 M_{\odot}$, $\phi_0 = -0.4\pi$, and $\gamma = 5/3$. The total number of SPH particles used in each simulation are 10^5 , and the termination time of each simulation is $4\Omega_*^{-1}$. Table 1 summarizes each model. Model 1a shows the standard TDE under the Newtonian potential, while Model 1b has the same simulation parameters as Model 1a, except that the star moves under the pseudo-Newtonian potential given by equation (10). Model 1c and 1d have the same parameters as Model 1a and Model 1b, respectively, but for $\beta = 5$. Model 2a has the same parameters as Model 1d except that the star is on an eccentric orbit, with $e = 0.8$. Model 2b is the same parameters as Model 2a except that the star moves under the Newtonian potential. Model 3a has the same parameters as Model 2a but for $e = 0.98$ and $\beta = 1$, and Model 3b has the same parameters as Model 3a but for $\beta = 5$.

3 TIDAL DISRUPTION OF STARS ON BOUND ORBITS

We first describe the evolution of a tidally disrupted star for standard TDEs ($e = 1$). Next, the process of tidal disruption for a star on a fairly eccentric orbit ($e = 0.98$) is presented. Finally, accretion disk formation in relatively low eccentricity TDEs ($e = 0.8$) is presented.

As an approaching star enters into the tidal disruption radius, its fluid elements become dominated by the tidal force of the black hole, while their own self-gravity and pressure forces become relatively negligible. The tidal force then produces a spread in specific energy of the stellar debris

$$\Delta\epsilon \approx \frac{GM_{\text{BH}}r_*}{r_t^2}. \quad (11)$$

The total mass of the stellar debris is defined with the differential mass distribution $m(\epsilon) \equiv dM(\epsilon)/d\epsilon$ by

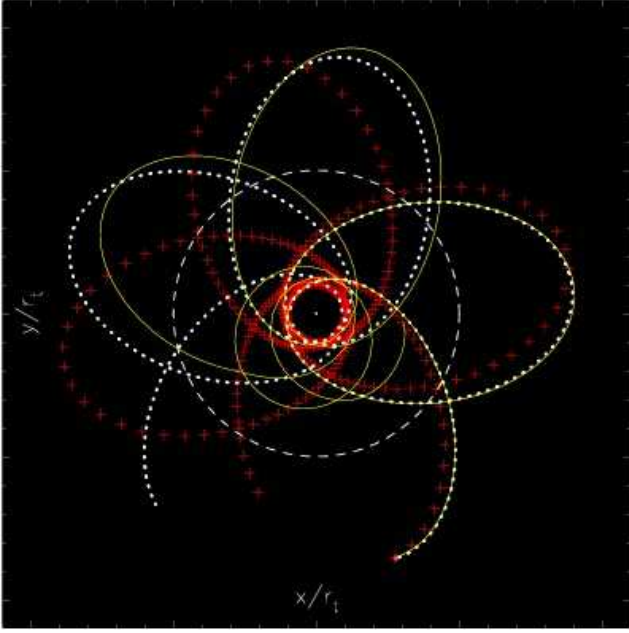


Figure 3. Motion of three particles with orbital parameters $(e, \beta) = (0.8, 5)$ in the x - y plane. Each axis is normalized by r_τ given by equation (5). The central point and dashed circle represent the black hole and tidal disruption radius, respectively. The small crosses, dotted line, and solid line show the geodesics in the Schwarzschild metric, orbits of a test particle under the pseudo-Newtonian potential given by equation (10), and orbits of a SPH particle in the simulation of Model 2a (see text of § 3.2), respectively.

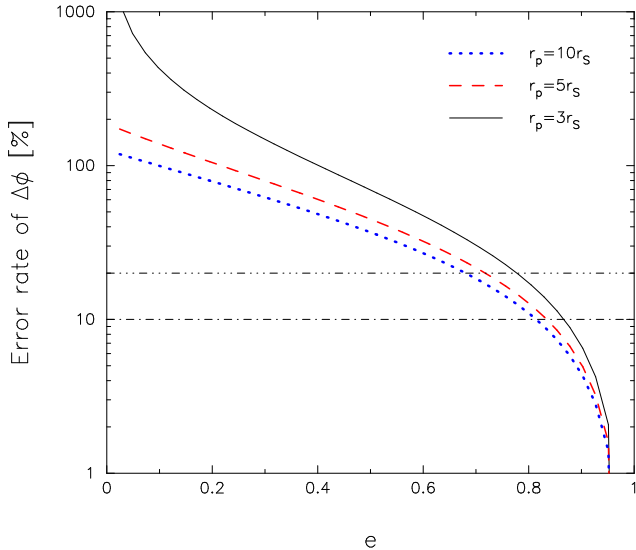


Figure 4. Dependence of error rate of precession angle $\Delta\phi$ on the eccentricity of a test particle moving under the pseudo-Newtonian potential given by equation (10). The solid line, dashed line, and dotted line show error rates of an orbit with $r_p = 3r_S$, $r_p = 5r_S$, and $r_p = 10r_S$, respectively. The horizontal dash-dotted line and dash-three-dotted line show the error cutoffs of 10% and 20%, respectively.

$$M(\epsilon) \equiv \int_{-\infty}^{\infty} m(\epsilon') d\epsilon'. \quad (12)$$

When a star is disrupted from a parabolic orbit, $m(\epsilon)$ will be centered on zero and distributed over $-\Delta\epsilon \leq \epsilon \leq \Delta\epsilon$.

Since the stellar debris with negative specific energy is bounded to the black hole, it returns to pericenter and will eventually accrete onto the black hole. If its specific energy is approximately equal to the specific binding energy, $\epsilon \approx -GM_{\text{BH}}/2a$ with the semi-major axis of the stellar debris a , the mass fallback rate is then defined by (e.g., Evans & Kochanek (1989))

$$\frac{dM}{dt} = \frac{dM(\epsilon)}{d\epsilon} \left| \frac{d\epsilon}{dt} \right| \quad (\epsilon < 0), \quad (13)$$

where

$$\frac{d\epsilon}{dt} = -\frac{1}{3}(2\pi GM_{\text{BH}})^{2/3} t^{-5/3}. \quad (14)$$

This is derived from the relationship between the orbital period and the specific energy:

$$t = \frac{\pi}{\sqrt{2}} \frac{GM_{\text{BH}}}{\epsilon^{3/2}}, \quad (15)$$

from Kepler's third law. The standard $dM/dt \propto t^{-5/3}$ scaling then arises with the assumption that $dM/d\epsilon$ is constant, or at least asymptotes to a constant value at late times. From equation (15), the orbital period of the most tightly bound orbit (t_{min}) and that of the most loosely bound orbit (t_{max}) are given by

$$t \rightarrow \begin{cases} t_{\text{min}} = (\pi/\sqrt{2}) (M_{\text{BH}}/m_*)^{1/2} \Omega_*^{-1} & (\epsilon = \Delta\epsilon) \\ t_{\text{max}} = \infty & (\epsilon = 0) \end{cases}. \quad (16)$$

Figs. 5-8 show the evolution of differential mass distributions and their corresponding mass fallback rates in Models 1a-1d. While the differential mass distribution is shown in panel (a), the mass fallback rate is shown in panel (b). In both panels, the solid line, dashed line, dot-dashed line, and dotted line represent the mass distributions and corresponding mass fallback rates at $t = 0.0$, $t = 0.37$, $t = 0.79$, and $t = 4.0$, respectively. Note that $t = 0.5$ corresponds to the time when the star reaches pericenter. In panel (b), the horizontal solid line denotes the Eddington rate:

$$\begin{aligned} \dot{M}_{\text{Edd}} &= \frac{1}{\eta} \frac{L_{\text{Edd}}}{c^2} \simeq 2.2 \times 10^{-2} \\ &\times \left(\frac{\eta}{0.1} \right)^{-1} \left(\frac{M_{\text{BH}}}{10^6 M_\odot} \right) M_\odot \text{yr}^{-1}, \end{aligned} \quad (17)$$

where $L_{\text{Edd}} = 4\pi GM_{\text{BH}} m_p c / \sigma_T$ is the Eddington luminosity with m_p and σ_T denoting the proton mass and Thomson scattering cross section, respectively, and η is the mass-to-energy conversion efficiency, which is set to 0.1 in the following discussion.

In Model 1a, the mass distribution broadens with time as the stellar debris is put on near-ballistic orbits by tidal interaction with the black hole. In panel (a), the central peak formed after $t \gtrsim 1.0$ is due to mass congregation, from the self-gravity of the stellar debris (in this scenario, the star is barely disrupted). The energy spread corresponds to $\Delta\epsilon$ before and after the tidal disruption. The corresponding mass fallback rates are proportional to $t^{-5/3}$ except for the solid line in panel (b). This is in good agreement with the literatures (Rees 1988; Evans & Kochanek 1989). The

slight deviation from t to the $-5/3$ power originates from the convexity around $\Delta\epsilon$ due to re-congregation of stellar mass under self-gravity (see Lodato et al. (2009)).

Model 1b has the same simulation parameters as Model 1a except that it adopts the pseudo-Newtonian potential. In panel (a) of Fig. 6, the final energy spread and the central peak are slightly wider and milder than those of Model 1a. This is because the energy imparted by the tidal force under the pseudo-Newtonian potential is slightly larger than that of the Newtonian potential. From equation (10), the energy spread under the pseudo-Newtonian potential is evaluated to be

$$\Delta\epsilon_{\text{PN}} \approx \left. \frac{dU(r)}{dr} \right|_{r=r_t} r_* = \Delta\epsilon \left[c_1 + \frac{1 - c_1}{[1 - c_2(r_S/2r_t)]^2} + 2c_3 \frac{r_S}{2r_t} \right]. \quad (18)$$

The expected energy spread $\Delta\epsilon_{\text{PN}} \sim 1.1\Delta\epsilon$ for $10^6 M_\odot$ is in good agreement with the simulated energy spread.

Model 1c has the same simulation parameters as Model 1a except for $\beta = 5$, while Model 1d has the same simulation parameters as Model 1c except for adopting the pseudo-Newtonian potential. For higher value of β than unity, the tidal forces acting on the star become stronger because the pericenter distance is smaller than the tidal disruption radius. According to equation (2) of Evans & Kochanek (1989), the energy spread of the stellar debris can be estimated to be $\beta^2\Delta\epsilon$, and should become $25\Delta\epsilon$ for Models 1c and 1d. In these two models, however, the energy spread is only about 1.4 times wider than that of standard model, showing that the energy spread weakly depends on β . This is in agreement with recent numerical (Guillochon & Ramirez-Ruiz 2012) and analytic work (Stone et al. 2012) that demonstrates the inaccuracy of the traditional formula for $\Delta\epsilon$, in place of which we have used the more accurate equation (11). Since the tidal disruption is less marginal as β is higher, the re-congregation of the mass due to self-gravity of the stellar debris is prevented. This leads to the mildly-sloped mass distribution, and therefore the peak of the mass fallback rate also smooths. There is no remarkable difference between Model 1c and Model 1d except that the energy spread of Model 1d is slightly wider than that of Model 1c following equation (18).

3.1 Eccentric tidal disruption

The specific orbital energy of a star on an eccentric orbit is given by

$$\epsilon_{\text{orb}} \approx -\frac{GM_{\text{BH}}}{2a_*} = -\frac{GM_{\text{BH}}}{2r_t} \beta(1 - e_*). \quad (19)$$

This quantity is less than zero because of the finite value of a_* , in contrast to the standard, parabolic orbit of a star. If ϵ_{orb} is less than $\Delta\epsilon$, all the stellar debris should be bounded to the black hole, even after the tidal disruption. The condition $\epsilon_{\text{orb}} = \Delta\epsilon$ therefore gives a critical value of orbital eccentricity of the star

$$e_{\text{crit}} \approx 1 - \frac{2}{\beta} \left(\frac{m_*}{M_{\text{BH}}} \right)^{1/3}, \quad (20)$$

below which all the stellar debris should remain gravitationally bound to the black hole (Amaro-Seoane et al. 2011). The critical eccentricity is evaluated to be $e_{\text{crit}} = 0.996$ for Model 2a and Model 3b, whereas $e_{\text{crit}} = 0.98$ for Model 3a.

For the eccentric TDEs, t_{min} and t_{max} are obtained by substituting $\epsilon = \Delta\epsilon \pm \epsilon_{\text{orb}}$ into equation (15). The orbital period of the most tightly bound orbit is given by

$$t_{\text{min}} = \frac{\pi}{\sqrt{2}} \frac{\Omega_*^{-1}}{\beta^{3/2}(1 - e_*)^{3/2}}. \quad (21)$$

The orbital period of the most loosely bound orbit t_{max} is estimated to be ∞ for $e_* \geq e_{\text{crit}}$, while t_{max} converges with

$$t_{\text{max}} = \frac{\pi}{\sqrt{2}} \Omega_*^{-1} \left[\frac{\beta(1 - e_*)}{2} - \left(\frac{m_*}{M_{\text{BH}}} \right)^{1/3} \right]^{-3/2} \quad (22)$$

for $e_* < e_{\text{crit}}$. The duration time of mass fallback for eccentric TDEs with $e_* < e_{\text{crit}}$ is thus predicted to be finite and can be written by

$$\Delta t = t_{\text{max}} - t_{\text{min}} = \frac{\pi}{\sqrt{2}} \frac{\Omega_*^{-1}}{[\beta(1 - e_*)]^{3/2}} \times \left(\left[\frac{1}{2} - \frac{1}{\beta(1 - e_*)} \left(\frac{m_*}{M_{\text{BH}}} \right)^{1/3} \right]^{-3/2} - 1 \right). \quad (23)$$

Evaluating this gives $\Delta t \approx 4.3\Omega_*^{-1}$ for Model 2a and $\Delta t \approx 207\Omega_*^{-1}$ for Model 3b, whereas $\Delta t \rightarrow \infty$ for Model 3a.

Figs. 9 and 10 show the evolution of differential mass distributions and corresponding mass fallback rates in Model 3a and Model 3b, respectively. The figure formats are the same as Figs. 5-8. The mass is not distributed around zero but around $-\Delta\epsilon$ in Model 3a, and around $-5\Delta\epsilon$ in Model 3b. This is because the specific energy of the initial stellar orbit is originally negative (see equation 19). It is clear from the negative shift of the mass distribution's center that most of the mass in Model 3a and all of the mass in Model 3b are bounded. As shown in panel (a) of Fig. 9, the resultant energy spread is slightly larger than we analytically expected. This suggests that the critical eccentricity is slightly smaller than the value in equation (20).

From equations (21) and (22), $t_{\text{min}} = 0.04\text{yr}$ and $t_{\text{max}} \rightarrow \infty$ for Model 3a, and $t_{\text{min}} = 0.0035\text{yr}$ and $t_{\text{max}} = 0.014\text{yr}$ for Model 3b. These values deviate from simulation results, because they were derived assuming a smaller spread in energy than in our simulations. Furthermore, t_{min} is shorter than that of the parabolic case. This makes the mass fallback rate about one order of magnitude higher. Notably, the mass accretion is completely finite in Model 3b and its rate is enhanced by about two orders of magnitude, because its timescale is much shorter than that of the standard model.

3.2 Accretion disk formation

Here we describe how an accretion disk forms rapidly around the black hole in Model 2a. The orbital angular momentum of a star passing inside the tidal disruption radius should be conserved before and after the tidal disruption, if there is no mechanism to redistribute the angular momentum. The orbits of the stellar debris can then be circularized by dissipation of orbital energy, primarily due to shocks from orbit crossing, which conserve orbital angular momentum. Debris semi-major axes will thus approach the circularization radius of the initial stellar orbit.

The specific energy and specific angular momentum of a test particle with the orbital parameters of Model 2a, moving under the pseudo-Newtonian potential, are given as

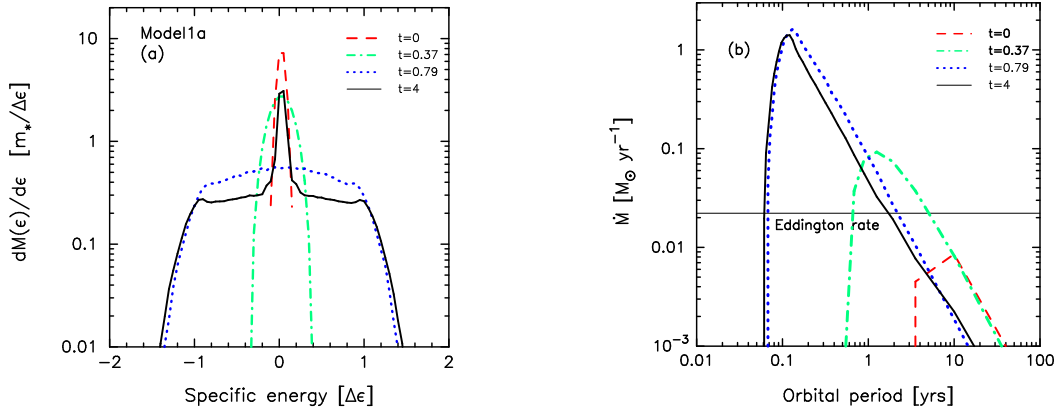


Figure 5. Evolution of differential mass distributions over specific energy of stellar debris and their corresponding mass-fall back rates, in Model 1a. In panel (a), the dashed line (red), dash-dotted (fairly green), dotted line (blue) and solid line (black) show the differential mass distributions measured at $t = 0$, $t = 0.37$, $t = 0.79$, and $t = 4$, respectively. The energy is measured in units of $\Delta\epsilon$ given by equation (11). In panel (b), the dash line (red), dashed-dotted line (fairly green), dotted line (blue), and solid line (black) show the mass fall-back rates measured at $t = 0$, $t = 0.37$, $t = 0.79$, and $t = 4$, respectively. Each mass fallback rate is evaluated by using each differential mass distribution represented in panel (a). The mass fallback rate and the orbital period are normalized by 1 solar mass per year and a year, respectively.

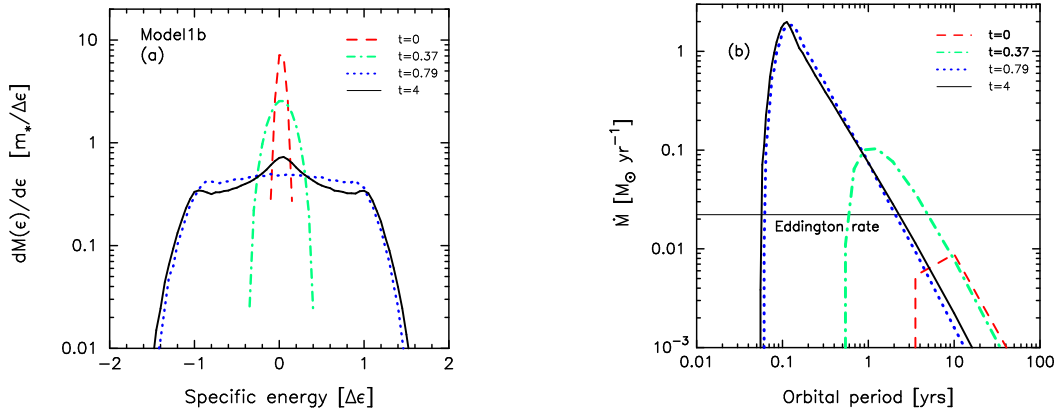


Figure 6. Same as Fig. 5, but for Model 1b.

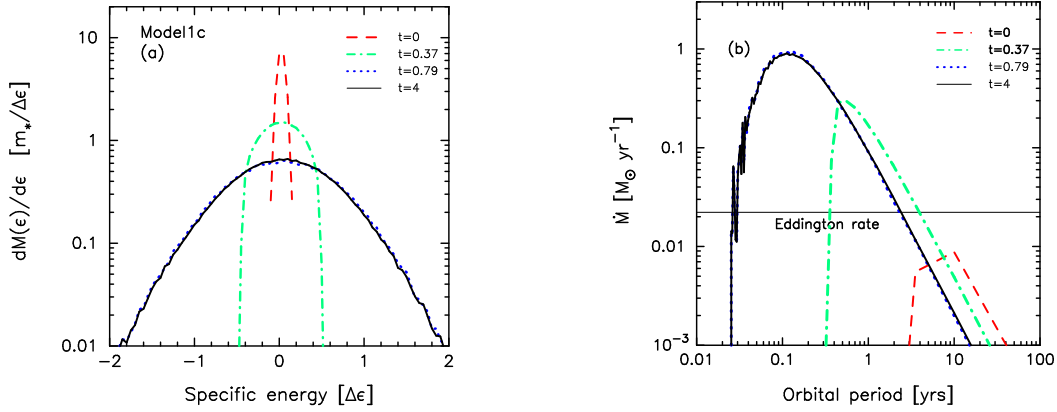


Figure 7. Same as Fig. 5, but for Model 1c.

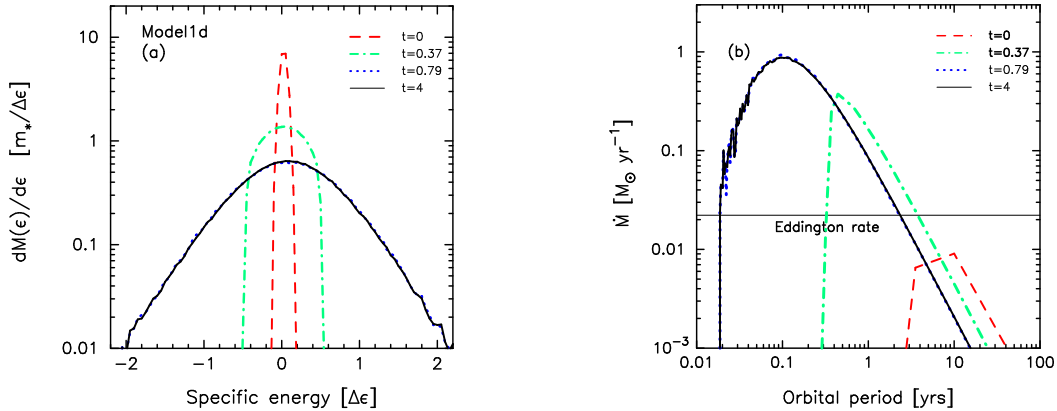


Figure 8. Same as Fig. 5, but for Model 1d.

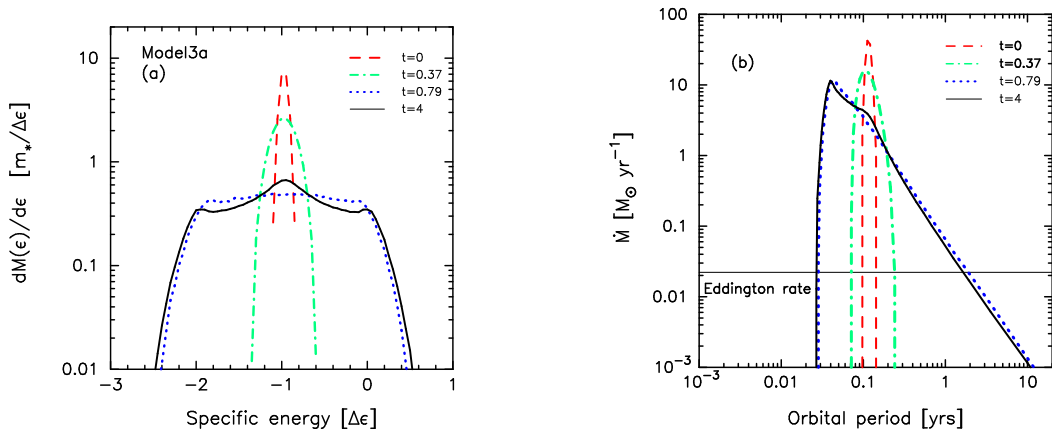


Figure 9. Same as Fig. 5, but for Model 3a.

$\epsilon_{\text{tp}} = -0.497$ and $l_{\text{tp}} = 0.714$, respectively, by substituting $(r_p, r_a) = (0.2r_t, 1.8r_t)$ with $(e, \beta) = (0.8, 5)$ into equations (9) and (10). Fig. 11 shows the evolution of the specific energy, specific internal energy, and the specific angular momentum in Model 2a. In panel (a), the solid line and the dashed line show the SPH specific energy and that of a test particle, respectively. The small inside panel shows the evolution of the specific internal energy, which is dissipated and radiated away after $t = 2.4\Omega^{-1}$ due to the shocks from self-intersections of the debris orbits induced by relativistic precession. Since the internal energy contributes negligibly to the total energy budget, the specific energy approximately equals the specific binding energy. On the other hand, panel (b) shows the evolution of the specific angular momentum normalized by l_{tp} . Its marginal fluctuation is a numerical error with a magnitude of 0.15%, indicating that the specific angular momentum is almost conserved. Assuming that the circularized disk has an axisymmetric Keplerian rotation, we can evaluate that the circularization radius $r_{\text{circ}} \approx 2.5r_p$.

Fig. 12 shows sequential snapshots of the surface density of stellar debris (projected on the x - y plane in five orders of magnitude, in a logarithmic scale) for Model 2a. The central small point, dashed circle, and dotted line show the black hole, tidal disruption radius, and orbits of a test particle moving under the pseudo-Newtonian potential, respectively. The run time is noted at the top-right corner in units of

Ω_*^{-1} , while the number of SPH particles are indicated at the bottom-right corner. The star is tidally disrupted before it passes through the first pericenter at $t = 0.5$. Afterward, the stellar debris expands along the orbit of the test particle as shown in panel (a) and (b). It is stretched towards the second pericenter as shown in panel (c). At the second pericenter, the stretched debris weakly intersects with the remnant of the debris in panel (d) and then reaches the second apocenter while continuing to expand, in panel (e). When it reaches the third pericenter in panel (f), two stretched orbits clearly cross over. The orbital energy is significantly dissipated by the shock from orbit crossing between the two stretched debris streams. This is consistent with the decrease of specific energy in panel (a) of Fig. 11. The stellar debris is therefore rapidly circularized as shown in panels (g) and (h). Finally, in panel (i), a disk like structure is formed around the black hole sufficiently inside the tidal disruption radius. Note that the number of SPH particles are slightly reduced from panel (e) to panel (i), since a very small fraction of the total number of SPH particles is accreted onto the black hole. The trajectory of a SPH particle picked out of this simulation for $0 \leq t \leq 4$ is drawn in the solid line of Fig. 3. The size of the accretion disk is in rough agreement with $r_{\text{circ}} \approx 2.5r_p$.

Although the pseudo-Newtonian potential does not accurately model the precession of near-circular orbits, we note that by the time the pseudo-Newtonian potential be-

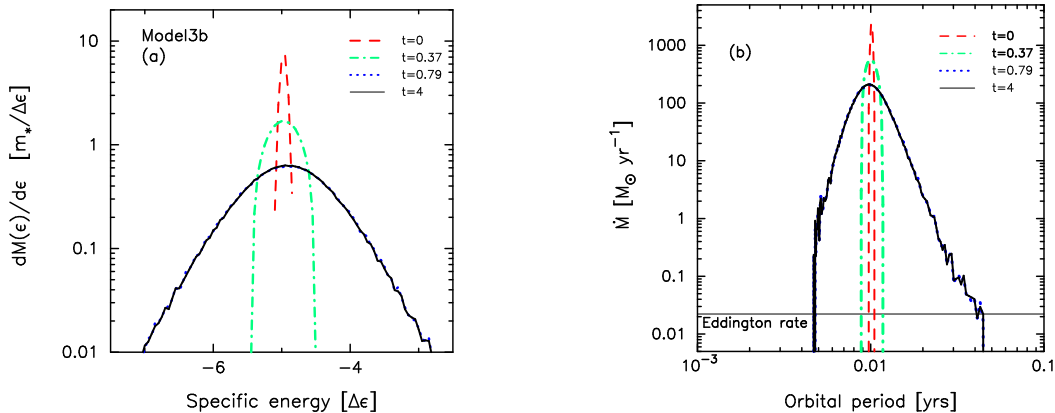


Figure 10. Same as Fig. 5, but for Model 3b.

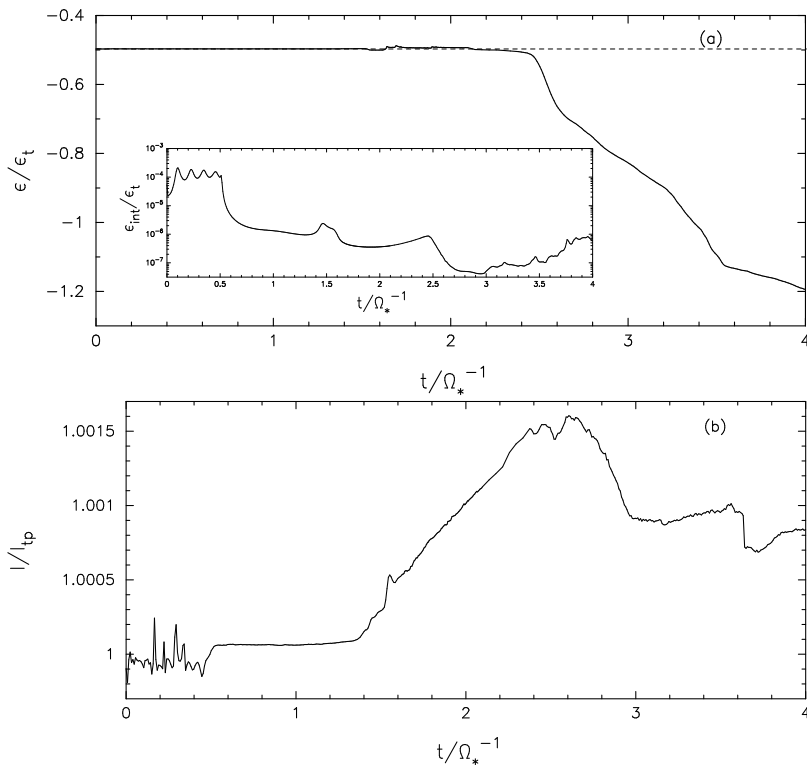


Figure 11. Evolution of the specific energy and specific angular momentum in Model 2a. In panel (a), the solid line and dashed line represent the specific energy of SPH particles and that of a test particle $\epsilon_{\text{tp}} = -0.497$, respectively. The small inside panel shows the evolution of the specific internal energy, ϵ_{int} . They are normalized by $\epsilon_t = GM/r_t$. Panel (b) shows the specific angular momentum normalized by $l_{\text{tp}} = 0.714$, which is the specific angular momentum of the initial stellar orbit.

comes significantly inaccurate, the debris streams have entered a regime of frequent orbit crossings, guaranteeing further rapid circularization. Furthermore, at a qualitative level the pseudo-Newtonian potential probably overestimates the circularization timescale, as it underestimates the true rate of relativistic precession for eccentric orbits. However, the pseudo-Newtonian potential still plays a crucial role in orbital circularization processes, because the motion of a test particle under the Newtonian potential take place in a closed path and therefore causes no orbit crossing. In order to test this, we have performed the simulation for Model 2b, which has the same simulation parameters as Model 2a except that

the Newtonian potential is adopted. Fig. 13 shows sequential snapshots of the surface density of stellar debris for Model 2b. It has the same format as Fig. 12. We note that there is no significant evidence for orbital crossings during the timescale of the simulation, since SPH particles orbit around the black hole on fixed eccentric orbits. This is also confirmed by the fact that the percentage change of specific orbital energy from $t=0$ to $t=4$ for Model 2b is less than 0.4%.

Fig. 14 shows the time-dependence of the number of SPH particles inside the tidal disruption radius N_{acc} and its first derivative (the mass capture rate). After the tidal dis-

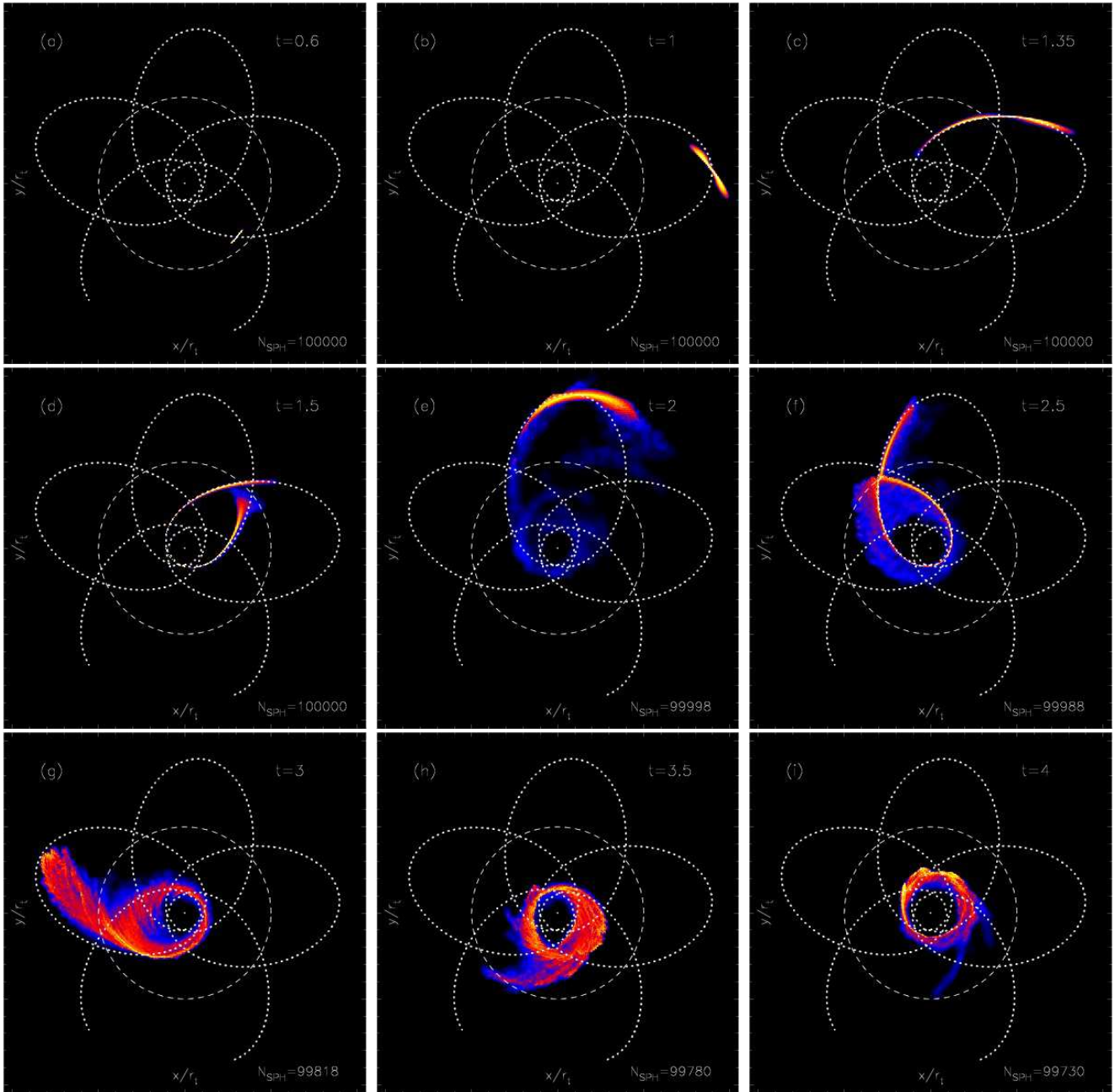


Figure 12. A sequence of snapshots of the tidal disruption process in Model 2a. They are from panel (a) to panel (i) in chronological order. Each panel shows a surface density projected on x - y plane in five orders of magnitude in a logarithmic scale for $0.6 \leq t \leq 4$, where t is in units of Ω_*^{-1} . The black hole is set at the origin. The run time is annotated at the top-right corner, while the number of SPH particles are indicated at the bottom-right corner. The dashed circle and dotted line indicate the tidal disruption radius and the orbits of a test particle moving under the pseudo-Newtonian potential given by equation (10), respectively.

ruption of the star, its orbit passes through the first apocenter, going completely outside of the tidal disruption radius. The first peak of N_{acc} in panel (a) comes when the debris streams pass from the first apocenter to the second apocenter via the second pericenter, and the stretched debris re-enters the tidal disruption radius. Part of it exits once more, but the fractional remaining part is still inside the tidal disruption radius. A sequence of these events can be seen in panels (c)-(e) of Fig. 12. The second peak of N_{acc} forms in panel (b). The stretched debris returns again to the

tidal disruption radius, moving toward the third pericenter. Afterwards, most of debris circularizes and remains inside of the tidal disruption radius.

Panel (b) of Fig. 14 shows the rate of mass being captured inside the tidal disruption radius. The first three peaks are formed as stellar debris passes in and out the tidal disruption radius, while the final peak shows the mass transfer rate to the accretion disk around the black hole. The mass transfer rate is also clipped from panel (b) to Fig. 15, as the mass accretion rate normalized by $1 M_{\odot} \text{ yr}^{-1}$. It is clear

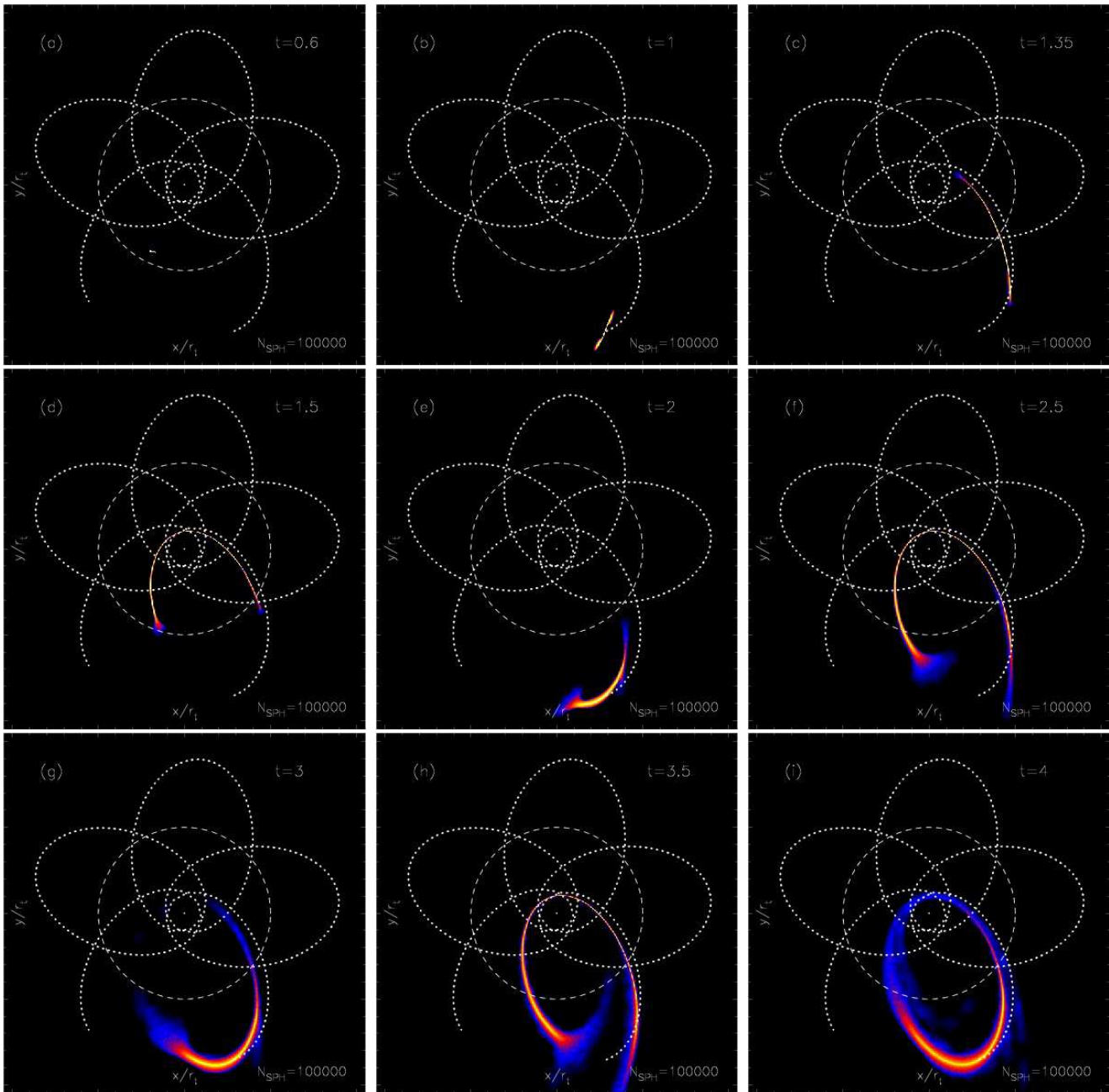


Figure 13. Same format as Model 2a but for Model 2b.

that the mass accretion rate has completely deviated from not only the canonical $t^{-5/3}$ law but also the accretion rate variation of the other highly eccentric TDEs (see Panel (b) of Figs. 9 and 10). The resultant accretion rate is more than five orders of magnitude higher than the Eddington rate (see equation 17). This shows that the accretion flow is extremely supercritical in the case of moderately eccentric TDEs.

Since the viscous timescale measured at r_{circ} is estimated to be $t_{\text{vis}} \sim 3.5 \times 10^3 (0.1/\alpha_{\text{SS}}) \Omega_*^{-1}$ where α_{SS} is the Shakura-Sunyaev viscosity parameter, the accretion flow is clearly in a non-steady state. Here, we assume that the accretion disk is a geometrically thick: $r_{\text{circ}}/H \sim 1$, where H is the disk scale height. Although the fate of the circularized debris is unclear because of much shorter simulation

time than the viscous timescale, the super-Eddington accretion flow will likely drive a powerful outflow (Ohsuga et al. 2005) as it becomes radiation-pressure dominated. This may increase the optical luminosity of the flare by orders of magnitude (Strubbe & Quataert 2009). It is even possible that a radiation-pressure supported envelope could be formed (Loeb & Ulmer 1997).

4 SOURCES OF ECCENTRIC TDES

Although the canonical source for TDEs is two-body scattering at parsec scales, a variety of alternate mechanisms exist. In this section we briefly review these, and highlight

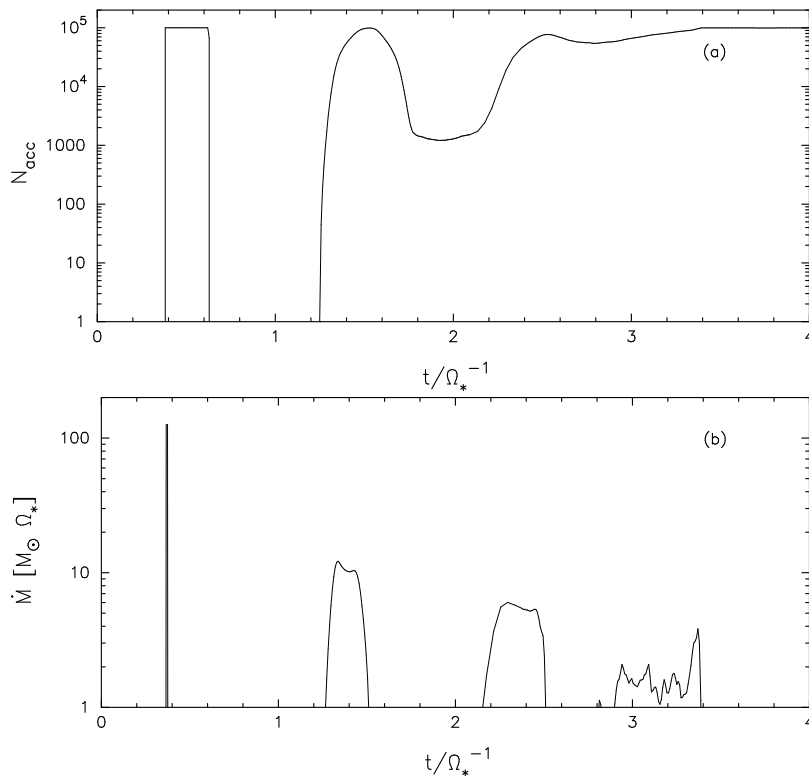


Figure 14. The number of SPH particles N_{acc} entering inside the tidal disruption radius over $0 \leq t \leq 4$ in panel (a) and its corresponding mass capture rate, which is measured by the number of particles entering inside the tidal disruption radius per unit time. In panel (b), the mass capture rate is normalized by M_\odot/Ω_*^{-1} , which corresponds to $8.9 \times 10^5 \dot{M}_{\text{Edd}}$ for a $10^6 M_\odot$ black hole with mass-to-energy conversion efficiency $\eta = 0.1$.

those which could supply stars at eccentricities $e < e_{\text{crit}}$ to their central SMBH.

- **Resonant relaxation:** at small spatial scales close to a SMBH, the approximately Keplerian potential causes stellar angular momentum to relax in a correlated, coherent way (as opposed to the uncorrelated changes from two-body relaxation). It has been suggested that the rapid changes in orbital eccentricity produced by resonant relaxation (RR) may enhance the TDE rate at small scales (Rauch & Ingalls 1998); however, recent work has indicated that the complicated interplay between RR and general relativistic precession gives rise to a “Schwarzschild barrier,” which quenches RR for stars with small semi-major axis (Merritt et al. 2011). RR is therefore unlikely to produce TDEs with $e < e_{\text{crit}}$.

- **Nuclear triaxiality:** conversely, the triaxial, non-Keplerian potential of a surrounding star cluster results in fewer constants of motion for stellar orbits; in particular, angular momentum is not conserved and some stars can wander arbitrarily close to the SMBH, eventually being disrupted (Merritt & Poon 2004). However, this effect only arises at large radii where the potential from the star cluster can induce a significant triaxial correction to the SMBH potential, and is therefore unlikely to produce low eccentricity TDEs.

- **A nuclear stellar disk:** there is a rotating stellar disk composed of young massive stars at the center of the Milky Way (Bartko et al. 2010). These stars orbit with moderate eccentricity around the supermassive black hole SgrA*. The

nonresonant relaxation timescale drops as a star cluster becomes flattened and disk-like, due to greater encounter rates between stars; simple estimates of the two-body eccentricity relaxation timescale in the Milky Way’s stellar disk ($\sim 5000 M_\odot$) find values $t_{\text{rlx}} \sim 4 \times 10^8$ yrs (Kocsis & Tremaine 2011). Assuming a typical stellar mass of $10 M_\odot$ gives a disk star TDE rate of $\sim 10^{-6} \text{ yr}^{-1}$, implying that if analogous disks are common in other galaxies, they could contribute nontrivially to the total TDE rate. However, in order to produce TDEs with $e < e_{\text{crit}}$, disk stars would need to be scattered in from $\sim \text{mpc}$ scales, implying that more compact disks than the Milky Way’s are needed to produce significantly eccentric TDEs.

- **Binary SMBHs:** A binary SMBH system will, for a period of $\sim 10^5$ yr to $\sim 10^6$ yr, see a TDE rate enhancement up to 10^{-1} yr^{-1} from a combination of chaotic orbital evolution and Kozai cycles (Ivanov et al. 2005; Chen et al. 2009). Recent work suggests that chaotic orbits in particular are the dominant contribution to the rate enhancement (Chen et al. 2011; Wegg & Nate Bode 2011). Most of the stellar flux originates from within one order of magnitude of the semimajor axis of the binary; since the inspiral of binary SMBHs stalls when the lower-mass secondary reaches a radius inside of which is contained its own mass in stars, a low binary mass ratio q will produce a flux of less eccentric TDEs. In particular, Fig. 17 of Chen et al. (2011) indicates that for $q = 1/81$ and a primary black hole mass of $10^7 M_\odot$, some stellar flux into the primary’s loss cone originates from spatial scales $\leq 10^{15}$ cm, which implies $e < e_{\text{crit}}$ even for

$\beta = 1$ events. However, the chaotic orbits which dominate the rate enhancement produce TDEs sampling a wide range of β (Merritt & Poon 2004), so the situation is even more favorable. Binary SMBHs on an eccentric orbit appear to produce even more TDEs from small apocenters. The “hardening radius” (the orbital radius within which the stellar cusp of the primary, larger SMBH contains the mass in stars of the secondary, smaller SMBH) effectively sets the scale at which stellar disruption rates are enhanced; to produce eccentric TDEs requires relatively low mass ratios ($< 1/50$) which could in some cases be characterized as SMBH-IMBH inspirals. Because binary SMBHs are expected to provide up to 10% of the total TDE rate (Wegg & Nate Bode 2011), it is important to note that a subset of these events may deviate from canonical “parabolic” light curves.

- **SMBH recoil:** the gravitational wave recoil accompanying a SMBH merger will scramble the orbits of surrounding stars and partially refill the kicked merger remnant’s loss cone, briefly increasing the TDE rate. If one considers the bulk of the stellar population surrounding the merging binary black holes, the excavation of a “binary loss cone” results in too few stars at small separation for the resulting burst of TDEs to involve any events with $e < e_{\text{crit}}$ (Stone & Loeb 2011). However, at low binary mass ratios, it is possible for mean motion resonances to migrate stars to small semimajor axes during the binary inspiral (Schnittman 2010; Seto & Muto 2010, 2011); any TDEs produced from this stellar subpopulation would have $e < e_{\text{crit}}$, and would be described by this paper.

- **Binary separation:** Recent theoretical studies on rates of tidal separation of binary stars by SMBHs suggest that a significant fraction of tidal disruption flares may occur from stars approaching the black hole from subparsec scales (Amaro-Seoane et al. 2011; Bromley et al. 2012). When a binary star passes sufficiently close to the black hole to be tidally separated (without immediate disruption of either component), one star becomes tightly bound to the black hole while the other is flung away at a high speed. The subsequent orbital evolution of the bound star will represent a competition between gravitational radiation and stellar relaxation processes. If gravitational radiation dominates, the orbit will circularize and spiral in, likely leading to a phase of steady mass transfer that is unlike the eccentric and violent disruptions which we have simulated in this paper. On the other hand, if stellar relaxational processes dominate, the star can eventually diffuse into the loss cone with a nonzero eccentricity that is still significantly smaller than that expected for TDEs generated by two-body relaxation at parsec scales. For a bound star with $r_p > r_t$ and semimajor axis a , living in a stellar cusp with density profile $\rho(r) \propto r^{-b}$, the eccentricity dividing gravitational-wave-dominated evolution from relaxation-dominated evolution is (Amaro-Seoane et al. 2011)

$$e_{\text{gw}} \approx 1 - 0.016 \times (8 \times 10^{-4})^{(2b-3)/5} (3-b)^{2/5} \times \left(\frac{M_{\text{BH}}}{10^7 M_{\odot}} \right)^{(8-b)/5} \left(\frac{a}{1000 \text{ AU}} \right)^{(2b-11)/5} \quad (24)$$

In practice, requiring $e_{\text{gw}} > e_{\text{crit}}$ for $a < r_t/(1 - e_{\text{crit}})$ is only possible for steep stellar cusps $b \approx 2$ and very low mass SMBHs ($M_{\text{BH}} \leq 10^{5.5} M_{\odot}$). A further complication is the presence of the Schwarzschild barrier, which may prevent stars with long gravitational wave inspiral timescales

from entering the loss cone. Stars bound to a SMBH from binary separation events can become TDEs with lower eccentricity than in the canonical scenario, but equation (24) implies their eccentricity will still tend to be greater than e_{crit} . On the other hand, equation (24) was derived assuming the Fokker-Planck diffusion limit for two-body relaxation, and anomalous diffusion from strong scattering events (Bar-Or et al. 2012) may allow violent tidal disruption of separated binaries even from eccentricities $e < e_{\text{gw}}$.

Of the possibilities we have considered, two stand out as particularly promising: TDEs generated as binary SMBHs harden and stall, and TDEs generated during the coalescence of binary SMBHs with a low mass ratio by stars that were brought inward via mean motion resonances. The first possibility may account for a significant fraction of the total TDE rate; the second possibility will be much less intrinsically common, but could serve as an electromagnetic counterpart to an eLISA/NGO¹-band gravitational wave signal. It is also possible that strong scatterings could lead to eccentric TDEs from the bound stars produced by tidal separation of stellar binaries. Other possible enhancements to theoretical TDE rates, such as perturbations from infalling giant molecular clouds, likely occur at too large of a spatial scale to create eccentric TDEs.

5 SUMMARY & DISCUSSION

We have carried out numerical simulations of mass fallback and accretion processes around a SMBH. Specifically, we have examined the tidal disruption of a star on a bound orbit, considering relativistic effects with a pseudo-Newtonian potential. Using a polytropic gas sphere as our initial conditions, we have considered both parabolic orbits ($e = 1.0$) and eccentric ones ($e = 0.8$ and 0.98), varying the penetration factor β as well.

We have found that a non-steady, non-axisymmetric accretion disk is formed around the black hole in the case of $e=0.8$ and $\beta = 5$. The formation of an accretion disk occurs as follows: a segment of the stellar debris returning to pericenter, and a different one exiting pericenter, intersect each other due to relativistic precession. The orbital energy is then dissipated by shocks due to orbit crossing. Since the orbital angular momentum of the stellar debris is conserved before and after the tidal disruption, the debris orbits are rapidly circularized during a few orbit crossings. This shows that the initial size of the accretion disk is only determined by the orbital angular momentum of the initial stellar orbit. In our simulations, the circularization radius is estimated as $r_{\text{circ}} \approx 2.5r_p$ where r_p is the pericenter distance. Furthermore, the expected accretion rate is extremely super-Eddington.

The striking difference between moderate-eccentricity simulations with and without relativistic precession highlights the importance of general relativistic effects for debris circularization. Specifically, very little energy dissipation was seen in Model 2b (Newtonian) of Table 1, while its pseudo-Newtonian equivalent, Model 2a, saw rapid accretion disk formation. For reasons of computational cost, we

¹ <http://www.elisa-ngo.org/>

did not follow the longer timescales required for debris circularization in other models, but in future work we hope to investigate if these results generalize to higher eccentricity and parabolic TDEs. Sufficiently rapid SMBH spin could delay disk formation, as Lense-Thirring torques will precess the orbital planes of individual debris streams and limit or prevent orbit-crossings. If a disk is able to eventually form, its luminosity will be periodically modulated by Lense-Thirring precession (e.g., Stone & Loeb 2012a). Even considering this complication, the energy dissipation process is crucial for determining the formation and structure of an accretion disk. In these exploratory simulations, we have adopted the polytropic equation of state instead of solving an energy equation. In a subsequent paper, we will study the detailed disk formation and structure by solving more realistic energy equations with and without a radiative cooling term.

Eccentric TDEs are a subpopulation of all TDEs, but a potentially interesting one. The two most promising means of producing them are in the dynamical friction stage of binary SMBHs, and immediately following gravitational wave-driven black hole coalescence. Both of these are especially interesting subsets of TDEs: the former occurs during a time of greatly enhanced TDE rates, when it may be possible for a single galaxy to produce multiple TDEs in ~ 10 yr, while the latter would serve as a delayed electromagnetic counterpart to a low-frequency gravitational wave signal. It is also possible that tidal separation of binary stars could produce TDEs of interestingly low-to-moderate eccentricity, if a large population of $M_{\text{BH}} \leq 10^{5.5} M_{\odot}$ SMBHs reside in steep stellar cusps. Eccentric TDEs are also of interest because of the relatively short delay time between disruption and disk formation, allowing numerical simulations to bypass costly apocenter passages and directly approach open problems in debris circularization. The pseudo-Newtonian potential proposed by Wegg (2012) is, however, not applicable for the very low eccentricities of fully circularized gas because it was derived with the assumption of small binding energy. Therefore, we hope to employ post-Newtonian corrections in a subsequent paper.

For eccentric stellar orbits, there is a critical value of the orbital eccentricity below which all stellar debris is bounded to the black hole. It can be seen from our simulations that the critical eccentricity is slightly lower than expected from our analytical predictions. This might be because of the effects of stellar structure on the tidal disruption. There are three important implications for lightcurves of eccentric TDEs:

- The mass fallback rate will not asymptote to $\dot{M} \propto t^{-5/3}$ at late times but be finite with cut-off time $t = t_{\text{max}}$.
- The lack of unbound debris will eliminate observational signatures associated with emission lines (e.g., Strubbe & Quataert 2009).
- A larger amount of mass will return to pericenter in a much shorter time than in the standard parabolic picture, considerably increasing the ratio of \dot{M}/M_{Edd} for the subsequent flare.

Even for eccentricities $e > e_{\text{crit}}$, the center of the differential mass distribution will shift in a negative direction, providing weaker versions of the above effects. These signatures should be searched for when large samples of TDE candi-

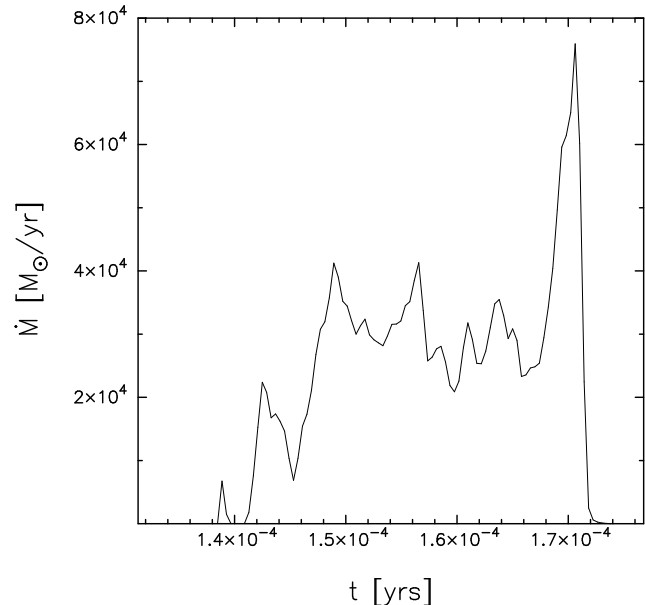


Figure 15. Mass accretion rate normalized by 1 solar mass per year, which corresponds to the final peak in panel (b) of Fig. 14.

dates from next generation optical transient surveys such as the Large Synoptic Survey Telescope² and next generation all-sky X-ray surveys such as extended Roentgen Survey with an Imaging Telescope Array³ become available.

ACKNOWLEDGMENTS

KH is grateful to Atsuo. T Okazaki, Takahiro Tanaka, and Shin Mineshige for helpful discussions and their continuous encouragement. The numerical simulations reported here were performed using the computer facilities of Yukawa Institute of Theoretical Physics, Kyoto University and Harvard-Smithsonian Center for Astrophysics, Harvard University. This work was supported in part by the Grants-in-Aid of the Ministry of Education, Science, Culture, and Sport and Technology [21540304, 22340045, 22540243, 23540271 KH], Education and Research Promotion Foundation in Kyoto University [KH], and NSF grant AST-0907890 and NASA grants NNX08AL43G and NNA09DB30A [NS, AL].

REFERENCES

- Amaro-Seoane, P., Coleman Miller, M., Kennedy, F. G., 2011, arXiv:1106.1429
 Bar-Or, B., Kupa, G., & Alexander, T. 2012, arXiv:1209.4594
 Bartko, H., Martins, F., Trippe, S., et al. 2010, ApJ, 708, 834
 Bate, M. R., Bonnel, I. A., Price, N.M., 1995, MNRAS, 277, 362

² <http://www.lsst.org/lst/>

³ <http://www.mpe.mpg.de/eROSITA>

- Benz W. 1990, in the Numerical Modeling of Nonlinear Stellar Pulsations: Problems and Prospects, ed. Buchler, R.J. (Dordrecht: Kluwer Academic Publishers), 269
- Benz, W., Bowers, R.L., Cameron, A.G.W., Press, W.H., 1990, ApJ, 348, 647
- Bromley, C. B., Kenyon, J. S., Geller, J. M., Brown, R. W., 2012, ApJ, 749, L42
- Bloom J. S. et al., 2011, Science, 333, 203
- Burrows D. N. et al., 2011, Nature 476, 421
- Carter, B., Luminet, J.-P., 1983, A&A, 121, 97
- Cannizzo, K. J., Lee, M. H., Goodman, J., 1990, ApJ, 351, 38
- Chen, X., Madau, P., Sesana, A., Liu, F. K., 2009, ApJ, 697, L149
- Chen, X., Sesana, A., Madau, P., Liu, F. K., 2011, ApJ, 729, 13
- Dogiel V. A., Chernyshov D. O., Yuasa T., Prokhorov D., Cheng K.-S., Bamba A., Inoue H., Ko C.-M., Kokubun M., Maeda Y., Mitsuda K., Nakazawa K., Yamasaki N. Y., 2009, PASJ, 61, 1099
- Donley J. L., Brandt W. N., Eracleous M., Boller T., 2002, AJ, 124, 1308
- Evans C.R., Kochanek C.S., 1989, ApJ, 346, L13
- Frank, J., Rees, M. J., 1976, MNRAS, 176, 633
- Genzel, R., Eisenhauer, F., Gillessen, S., 2010, Reviews of Modern Physics, 82, 3121
- Gezari S., et al., 2012, Nature, 485, 217
- Greiner J., Schwarz R., Zharikov, S., et al., 2000, A&A, 362, L25
- Grupe D., Thomas H.-C., Leighly, K. M., 1999, A&A, 350, L31
- Guillochon, J., & Ramirez-Ruiz, E. 2012, arXiv:1206.2350
- Halpern J. P., Gezari S., Komossa S., 2004, ApJ, 604, 572
- Hayasaki, K., Mineshige, S., Sudou, H., 2007, PASJ, 59, 427
- Ivanov, P. B., Polnarev, A. G., Saha, P., 2005, MNRAS, 358, 1361
- Kocsis, B., & Tremaine, S. 2011, MNRAS, 412, 187
- Komossa S., Bade N., 1999, A&A, 343, 775
- Komossa, S. et al., 2004, ApJ, 603, L17
- Komossa, S., Merritt, D., 2008, ApJ, 683, L21
- Landau, L. D., Lifshitz, E. M., 1969, Mechanics
- Lodato G., King A. R., Pringle J. E., 2009, MNRAS, 392, 332
- Lodato, G., & Rossi, E. M. 2011, MNRAS, 410, 359
- Loeb, A., Ulmer, A., 1997, ApJ, 489, 573
- Madigan, A.-M., Hopman, C., & Levin, Y. 2011, ApJ, 738, 99
- Magorrian, J., Tremaine, S., 1999, MNRAS, 309, 447
- Maksym, P. W., Ulmer, P. M., Eracleous, M., 2010, ApJ, 722, 1035
- Merritt, D., & Poon, M. Y. 2004, ApJ, 606, 788
- Merritt, D., Alexander, T., Mikkola, S., & Will, C. M. 2011, PRD, 84, 044024
- Miralda-Escudé, J., Kollmeier, J. A., 2005, ApJ, 619, 30
- Ohsuga, K., Mori, M., Nakamoto, T., Mineshige, S., 2005, ApJ, 628, 368
- Okazaki A.T., Bate M.R., Ogilvie G.I., Pringle J.E., 2002, MNRAS, 337, 967
- Phinney E. S., 1989, In M. Morris (ed.) The Center of the Galaxy, vol. 136 of IAU Symposium, 543?553
- Paczyński B., Wiita, P., 1980, A&A, 88, 23
- Rauch, K. P., & Ingalls, B., 1998, MNRAS, 299, 1231
- Rees M. J., 1988, Nature, 333, 523
- Schnittman, J. D. 2010, ApJ, 724, 39
- Seto, N., & Muto, T. 2010, PRD, 81, 103004
- Seto, N., & Muto, T. 2011, MNRAS, 415, 3824
- Stone, N., Sari, R., Loeb, A., 2012, in prep.
- Stone, N., Loeb, A., 2011, MNRAS, 412, 75
- Stone, N., Loeb, A., 2012, Physical Review Letters, 108, 061302
- Stone, N., Loeb, A., 2012, MNRAS, 422, 1933
- Strubbe, L. E., Quataert, E., 2009, MNRAS, 400, 2070
- van Velzen S. et al., 2011, ApJ, 741, 73
- Wang, J., Merritt, D., 2004, ApJ, 600, 149
- Wegg C., 2012, ApJ, 749, 183
- Wegg, C., Nate Bode, J., 2011, ApJ, 738, L8
- Zauderer B. A. et al., 2011, Nature 476, 425
- Zhao, H., Haehnelt, M. G., & Rees, M. J. 2002, NA, 7, 385